

Computations of a Compressible Turbulent Flow in a Rocket Motor-Chamber Configuration with Symmetric and Asymmetric Injection

W.A. El-Askary^{1,2}, A. Balabel², S.M. El-Behery² and A. Hegab³

Abstract: In the present paper, the characteristics of compressible turbulent flow in a porous channels subjected to either symmetric or asymmetric mass injection are numerically predicted. A numerical computer-program including different turbulence models has been developed by the present authors to investigate the considered flow. The numerical method is based on the control volume approach to solve the governing Reynolds-Averaged Navier-Stokes (RANS) equations. Turbulence modeling plays a significant role here, in light of the complex flow generated, so several popular engineering turbulence models with good track records are evaluated, including five different turbulence models. Numerical results with available experimental data showed that the flow evolves significantly with the distance from the front wall such that different regimes of flow development can be observed. The comparison between these computational models with experimental data for the axial velocity profiles and turbulent stresses is performed. The best numerical results are obtained from the shear-stress transport $k - \omega$ model (SST $k - \omega$) and $v^2 - f$ turbulence models as well. Although the $v^2 - f$ turbulence model generates fair results compared to the experimental ones, it needs little bit improvement to be reliable to treat this kind of complex flows. However, because of the high cost and long computation time required with using either the family of $k - \omega$ or $v^2 - f$ as well as the Reynolds Stress Model (RSM), the family of $k - \epsilon$ turbulence model still produces the behavior of turbulent flow in such complex turbulence structure with lowest cost and fair results.

Keywords: RANS; turbulence models; turbulence transpiration; porous wall; mass injection

¹ Corresponding author, Tel.: (Mobil) +2-01005255817; (home) +2-048-3486965; Fax: +2-048-2235695 Email address: wageeh_elaskary@yahoo.com

² Mechanical Power Engineering Department, Faculty of Engineering, Menoufiya University, Shebin El-Kom, Egypt

³ Professor and Head of Mechanical Engineering Department, King Abdul-Aziz University, Faculty of Engineering, Rabigh

1 Introduction

Flows through porous channels with wall injection are encountered in many engineering applications such as transpiration cooling, boundary-layer control, and the combustion induced flow-field in solid rocket motors (SRM). The internal flow development inside the combustion chamber of a solid rocket plays an essential role in motor design and operation. The mean velocity field and the turbulence characteristics have a strong-direct impact on many physical processes occurring within the motor such as the internal ballistics and erosive burning, the convective heat transfer to the thermal protection, the motion of alumina droplets and subsequent slag deposition at motor aft-end. Flow in the core of a SRM is unusual form of wall turbulence because the turbulence is created by the release of gas normal to the wall. Turbulence effects significantly influence the flow processes in proximity of the combustion surface. A full treatment of this region would include the modeling and resolution of complex physical and chemical phenomena which take place during the solid propellant combustion process. This process occurs in a very thin layer $O(1 \text{ mm})$ scale above the combustion surface. For simplicity, most of the experimental and numerical simulations mimics the burning surface as a porous wall through which mass injection occurs at a given total temperature.

The structure of the internal flow in a SRM is very important to the stability and the operation of the motor. The flow in the chamber can be simulated by a channel with fluid injection through permeable walls. This type of flow evolves significantly with respect to the distance from the head end of the duct. Different flow regimes can be observed depending on the injection mass flow rate or the injection Reynolds number at the porous wall. In the first regime the velocity field is developed according to the laminar theory. The second flow regime is characterized by the development of turbulence and the transition process of the mean axial velocity when a critical turbulence threshold is attained; see Ciucci; Iaccarino; Moser; Najjar; Durbin (1998).

The injection-driven flow in a cylindrical port rocket motor (i.e., with a closed end) is significantly different from the flow in a pipe with or without porous walls. Mass addition from the wall in injection-driven flows is usually quite large. As a result, the velocity profile for an injection-driven flow comes essentially from a balance between the pressure gradient and inertial forces, in contrast with a pipe flow where the velocity profile is determined by a balance of viscous stresses and pressure forces. The experiments performed by Culick (1966) and Dunlap; Willoughby; Hermsen (1974) showed that the mean flow field is accurately represented by a cosine transverse distribution for the axial velocity in the forward region of a cylindrical port rocket chamber. However, these investigations were performed at large injection rates, revealed that the transition from laminar to turbulent flow was car-

ried out over most of the chamber.

Because of the progress in computing power, channel flows with fluid injection through porous walls have been studied numerically by several authors. Traineau; Hervat; Kuentzmann (1986) conducted cold flow simulations of a two-dimensional nozzleless motor, and Dunlap; Blackner; Waugh; Brown; Willoughby (1990) investigated the internal flow in a cylindrical port rocket chamber. In both cases, injection rates were considerably high. Beddini (1986) performed numerical studies of the injection-driven flow in a duct using a parabolic form of the Navier-Stokes equations together with a full Reynolds stress turbulence model. In that work, turbulent fluctuations at the surface, described as "pseudo-turbulence", were introduced for the first time.

Several numerical investigations of flows without fluid injection and with fluid injection at the wall have been performed in the past. Sabnis; Gibeling; McDonalds (1989) carried out a simulation of the test motor geometry employed by Dunlap; Blackner; Waugh; Brown; Willoughby (1990) using the $k - \varepsilon$ turbulence model of Jones; Launder (1972) and based on the computation method described in Patankar (1980). A large over-prediction of the turbulence intensity profiles was obtained. Sabnis; Gibeling; McDonalds (1989) adopted a modified form of the same turbulence model and compared their results with the data of Traineau; Hervat; Kuentzmann (1986); some improvements were achieved, but a considerable discrepancy in the turbulence data remained.

With much more increase in computer power and advancements in CFD in recent years, both LES and DNS analyses of turbulent flows with transpiration walls have been performed. Moin (1982) and Piomelli; Moin; Ferziger (1991) applied LES to compute the flow in a channel with a uniform injection at the lower wall and an equal suction at the opposite wall, to simulate the experiment carried by Andersen; Kays; Moffat (1975) with low injection rates.

Liou; Lien (1995) and Liou; Lien; Hwang (1998) performed a numerical simulation using a two-dimensional large eddy simulations approaches without explicit subgrid scale modeling. Although their results were in general in good agreement with the experimental data of Traineau; Hervat; Kuentzmann (1986), turbulence intensities were somewhat under-predicted in the second half of the channel. The results of Liou; Lien; Hwang (1998) showed that the large eddy structures play an important role in the flow. Recently, Apte; Yang (2001) introduced a solution for the three-dimensional Navier-Stokes equations using a compressible version of a dynamic Smagorinsky model for simulating this flow. The vortex-stretching and rolling mechanisms of the flow were well reproduced. They revealed that the large eddy simulation must be three-dimensional for predicting the Reynolds stresses.

Generally, the problem of porous-wall channel with mass addition through the porous wall needs more attention; in one hand, to understand the behavior of such complex flow and in the other hand to find the suitable turbulence models for such configuration. In the present paper, RANS simulation using five different turbulence models, including the standard $k - \varepsilon$, SST $k - \omega$, Reynolds stress, extended $k - \varepsilon$ and $v^2 - f$ turbulence models are performed to understand the nature of the flow field in a channel with permeable walls.

The aim of the present study is to assess the applicability of different turbulence models in a numerical code developed by the present authors, to the simulation of such class of flows; and to improve the understanding of the fluid physics governing this turbulent flow and to obtain some physical insights on the near-wall turbulent structures. To this end, the present work has comprised two separate but complementary activities. In the first activity, numerical simulation is performed to simulate a duct with asymmetrical injection and freely discharges to atmosphere; corresponding to available experimental work in literature. The simplest and successful turbulence model will be chosen for the second more complex activity concerning a rocket motor chamber with realistic flow conditions, previously measured.

2 Mathematical model

The time-averaged conservation equations can be written for compressible steady flow as follows:

Time-Averaged Continuity Equation

$$\frac{\partial}{\partial x_i}(\rho u_i) = 0 \quad (1)$$

Time-Averaged Momentum Equation

$$\frac{\partial}{\partial x_j}(\rho u_i u_j) = -\frac{\partial p}{\partial x_i} + \frac{\partial}{\partial x_j} \left[\mu \left(\frac{\partial u_i}{\partial x_j} + \frac{\partial u_j}{\partial x_i} - \frac{2}{3} \delta_{ij} \frac{\partial u_l}{\partial x_l} \right) \right] + \frac{\partial}{\partial x_j} (-\rho \overline{u'_i u'_j}) \quad (2)$$

Time-Averaged Energy Equation

$$\frac{\partial [u_j(\rho e + p)]}{\partial x_j} = \frac{\partial}{\partial x_j} \left[(\lambda + C_p \mu_t / \text{Pr}_t) \frac{\partial T}{\partial x_j} - u_i (\rho \overline{u'_i u'_j}) \right] \quad (3)$$

Where, u_i denotes the mean velocities and u'_i and u'_j are the turbulence velocities, ρ is the density, p is the pressure, λ is the thermal conductivity, C_p is the specific heat at constant pressure, Pr_t is the turbulent Prandtl number and μ is the laminar viscosity. The total energy per unit volume is defined as: $\rho e = \rho C_v T + 0.5 \rho u_i^2$, where C_v is the specific heat at constant volume and T is the temperature.

Equations 1 and 2 have the same general form as the instantaneous Navier-Stokes equations, with the velocities and other scalar variables now representing ensemble-averaged (or time-averaged) values. Additional terms now appear that represent the effects of turbulence (Reynolds stresses; $-\rho \overline{u'_i u'_j}$). These stresses must be modeled in order to close Equations 2 and 3. For compressible flow, equations 1, 2 and 3 can be interpreted as Favre-averaged conservation equations, with the velocities representing mass-averaged values. The Reynolds-averaged conservation equations for steady compressible turbulent flow along with a turbulence model are coupled with the equation of state, $p = \rho RT$ to close the system of equations.

2.1 Turbulence modeling

In industrial CFD applications, RANS modeling remains one of the main approaches when dealing with turbulent flows. During the last few decades, a great variety of RANS turbulence models are developed. Modeling approaches in the context of RANS have shown different degrees of success in various engineering applications, spanning from mixing-length models, linear and nonlinear eddy viscosity models to algebraic and differential Reynolds stress models with a hierarchy of increasing complexity in the modeling formulation and related CFD implementations. For an appropriate compromise between computational efficiency and accuracy, only a few of RANS models have been popularized in the aerodynamic CFD applications. The Reynolds-averaged approach to turbulence modeling requires appropriate modeling of the Reynolds stresses in Equation 2. A common method employs the Boussinesq hypothesis, see Hinze (1975) to relate the Reynolds stresses to the mean velocity gradients:

$$-\rho \overline{u'_i u'_j} = \mu_t \left(\frac{\partial u_i}{\partial x_j} + \frac{\partial u_j}{\partial x_i} \right) - \frac{2}{3} (\rho k + \mu_t \frac{\partial u_k}{\partial x_k}) \delta_{ij} \quad (4)$$

where, δ_{ij} is the Kronecker's delta function ($\delta_{ij}=1$ if $i = j$ and $\delta_{ij}=0$ if $i \neq j$), k is the turbulent kinetic energy. The Boussinesq hypothesis is used in the $k - \varepsilon$, $v^2 - f$ and SST $k - \omega$ models. The advantage of this approach is the relatively low computational cost associated with the computation of the turbulent viscosity, μ_t . In the case of the $k - \varepsilon$ and SST $k - \omega$ models, two additional transport equations (for the turbulence kinetic energy, k , and either the turbulence dissipation rate, ε , or the specific dissipation rate, ω) are solved, and μ_t is computed as a function of k and ε or ω . The disadvantage of the Boussinesq hypothesis as presented is that it assumes μ_t is an isotropic scalar quantity, which is not strictly true.

The alternative approach, embodied in the Reynolds-stress model (RSM), is to solve transport equations for each of the terms in the Reynolds stress tensor. An additional scale-determining equation (normally for ε) is also required. This means

that five additional transport equations are required in 2D flows and seven additional transport equations must be solved in 3D flows.

In many cases, models based on the Boussinesq hypothesis perform very well, and the additional computational expense of the Reynolds stress model is not justified. However, the RSM is clearly superior for situations in which the anisotropy of turbulence has a dominant effect on the mean flow. Such cases include highly swirling flows and stress-driven secondary flows.

The numerical method considered in the present developed code is based on the finite volume approach. The discretised equations, along with the boundary conditions, are solved using a staggered grid. Using the solver, the conservation of mass and momentum are solved sequentially and a pressure-correction equation is used to ensure the conservation of momentum and the conservation of mass (continuity equation). Five different turbulence models, i.e. the standard $k - \varepsilon$ model, the shear-stress transport $k - \omega$ model (SST $k - \omega$), the Reynolds stress models (RSM), are employed. The implementation of the modified version of $k - \varepsilon$ by Chen; Kim (1987) and the modified $v^2 - f$ (V2F turbulence model of Durbin (1995)) are also considered. A brief discussion of these turbulence models are presented in the following subsections.

2.1.1 Standard $k - \varepsilon$ of Launder and Spalding (SKE)

The standard $k - \varepsilon$ model is derived by assuming that the flow is fully turbulent and the effects of molecular viscosity are negligible (Launder; Spalding (1974)). For the locations near walls, the standard $k - \varepsilon$ model, demands an additional sub-model to account the effects of molecular viscosity. In this situation, wall functions based on semi-empirical formulas and functions are usually employed.

2.1.2 Shear stress transport $k - \omega$ model (SST $k - \omega$)

The SST $k - \omega$ model was developed by Menter (1994), which employs the standard $k - \omega$ model of Wilcox (1998) in the near-wall region and the transformed $k - \varepsilon$ model in the far-wall region. The standard $k - \omega$ model is derived based on the turbulence kinetic energy (k) and the specific dissipation rate (ω), which is defined as the ratio of ε to k (Wilcox (1998)). The definition of the turbulent viscosity is modified to account for the transport of turbulent shear stress.

2.1.3 Reynolds stress model (RSM)

The RSM does not employ the Boussinesq hypothesis to relate the Reynolds stresses to the mean velocity gradients. However, the Reynolds stresses are solved in a transport equation for each of the terms in the Reynolds stress tensor; see Launder; Reece; Rodi (1975).

2.1.4 Extended $k - \varepsilon$ closure of Chen and Kim

For the closure of the governing equations using the extended $k - \varepsilon$ closure of Chen; Kim (1987) (Chen-Kim), the transport equation of the turbulent kinetic energy can be written as:

$$\frac{\partial}{\partial x_j}(\rho u_j k) = \frac{\partial}{\partial x_j} \left[\left(\mu + \frac{\mu_t}{\sigma_k} \right) \frac{\partial k}{\partial x_j} \right] + \rho(P_r - \varepsilon) \quad (5)$$

where P_r and ε represent the production rate and the dissipation rate of the turbulent kinetic energy, k , respectively, and σ_k is a modeling constant. The production rate is related to the mean strain of the velocity field through the Boussinesq assumption. That is,

$$P_r = \mu_t S^2 \quad (6)$$

where S is defined as:

$$S = \sqrt{\frac{1}{\rho} \left(\frac{\partial u_j}{\partial x_i} + \frac{\partial u_i}{\partial x_j} - \frac{2}{3} \delta_{ij} \frac{\partial u_k}{\partial x_k} \right) \frac{\partial u_i}{\partial x_j}} \quad (7)$$

For the dissipation rate equation, two time scales are included to allow the dissipation rate to respond to the mean strain more effectively than that of the standard $k - \varepsilon$ model.

This is the major improvement of the present $k - \varepsilon$ model for complex turbulent flow problems. The time scales included in the present model are: the production range time scale, k/P_r , and the dissipation rate time scale, k/ε . The final expression of the dissipation rate transport equation is given as (Chen; Kim (1987)):

$$\frac{\partial}{\partial x_j}(\rho u_j \varepsilon) = \frac{\partial}{\partial x_j} \left[\left(\mu + \frac{\mu_t}{\sigma_\varepsilon} \right) \frac{\partial \varepsilon}{\partial x_j} \right] + \rho \left(C_{1\varepsilon} P_r \frac{\varepsilon}{k} - C_{2\varepsilon} \frac{\varepsilon^2}{k} + C_{3\varepsilon} \frac{P_r^2}{k} \right) \quad (8)$$

The last term of the past equation represents the energy transfer rate from large scale turbulence to small scale turbulence controlled by the production range time scale and the dissipation rate time scale. The net effect of the present energy transfer function enhances the development of ε when the mean strain is strong, or large production rate, and the generation of ε is suppressed when the mean strain is weak, or small production rate. Consequently, as the model constants are carefully tuned, the present formulation enables the dissipation rate to respond to the mean flow field more rapidly so as to control the development of the turbulent kinetic energy more effectively. The model constants are: $\sigma_k = 0.75$; $\sigma_\varepsilon = 1.15$; $C_{1\varepsilon} = 1.15$; $C_{2\varepsilon} = 1.9$; $C_{3\varepsilon} = 0.25$.

2.1.5 V2F turbulence model (modified $v^2 - f$)

In essence the $v^2 - f$ model introduced by Durbin (1995) extends the standard $k - \varepsilon$ model to low-Reynolds number flow regions. This is realized by modifying the eddy viscosity formulation and solving two additional partial differential equations: an equation describing the transport of the turbulent intensity normal to the streamlines v^2 and an elliptic relaxation equation for f . The latter models the effect of the pressure-strain term.

In the present work the modified version of $v^2 - f$ model of Lien; Kalitzen (2001) and successfully used recently by Pecnik; Iaccarino (2007) will be considered. The distinguishing feature of the $v^2 - f$ model is its use of the velocity scale, v^2 instead of the turbulent kinetic energy, k , for evaluating the eddy viscosity. v^2 , which can be thought of as the velocity fluctuation normal to the streamlines, has shown to provide the right scaling in representing the damping of turbulent transport close to the wall, a feature that k does not provide. The turbulent viscosity is given by:

$$\mu_t = \rho C_\mu v^2 T \quad (9)$$

where T is the turbulent time scale and given by:

$$T = \max\left[\frac{k}{\varepsilon}, 6\sqrt{\frac{\mu}{\rho\varepsilon}}\right] \quad (10)$$

The standard $k - \varepsilon$ equations read

$$\frac{\partial}{\partial x_j}(\rho u_j k) = \frac{\partial}{\partial x_j} \left[\left(\mu + \frac{\mu_t}{\sigma_k} \right) \frac{\partial k}{\partial x_j} \right] + \rho(P_r - \varepsilon) \quad (11)$$

$$\frac{\partial}{\partial x_j}(\rho u_j \varepsilon) = \frac{\partial}{\partial x_j} \left[\left(\mu + \frac{\mu_t}{\sigma_\varepsilon} \right) \frac{\partial \varepsilon}{\partial x_j} \right] + \frac{\rho}{T} (C_{1\varepsilon} P_r - C_{2\varepsilon} \varepsilon) \quad (12)$$

The v^2 transport equation is

$$\frac{\partial}{\partial x_j}(\rho u_j v^2) = \frac{\partial}{\partial x_j} \left[\left(\mu + \frac{\mu_t}{\sigma_k} \right) \frac{\partial v^2}{\partial x_j} \right] + \rho \left(k f - 6 v^2 \frac{\varepsilon}{k} \right) \quad (13)$$

and the elliptic-relaxation equation f can be represented as:

$$L^2 \frac{\partial^2 f}{\partial x_j^2} - f = \frac{1}{T} \left[(C_1 - 6) \frac{v^2}{k} - \frac{2}{3} (C_1 - 1) \right] - C_2 \frac{P_k}{k} \quad (14)$$

and the turbulent length scale L is determined from the values of k and ε as follows:

$$L = C_L \max\left[\frac{k^{3/2}}{\varepsilon}, C_\eta \frac{(\mu/\rho)^{3/4}}{\varepsilon^{1/4}}\right] \quad (15)$$

The constants of the model are given as follows; see Lien; Kalitzen (2001):

$$\begin{aligned}
 C_\mu &= 0.22, \quad \sigma_k = 1, \quad \sigma_\varepsilon = 1.3, \\
 C_{1\varepsilon} &= 1.4(1 + 0.05\sqrt{k/v^2}); \quad C_{2\varepsilon} = 1.9, \\
 C_1 &= 1.4; \quad C_2 = 0.3; \quad C_L = 0.23; \quad C_\eta = 70.
 \end{aligned}
 \tag{16}$$

As noticed, all model constants are completely wall-distance independent.

The above system of equations, including the conservation equations and the turbulence model equations, is solved by the numerical method based on the control volume approach proposed by Patankar (1980). The governing equations are discretised using hybrid scheme for all variables except the density, which is interpolated using upwind scheme in order to obtain a linear system of algebraic equations. The system of equations is solved using the TDMA described in Patankar (1980). An important step of the above numerical procedure is the linearization of the source terms that vary according to the equations considered. The solution is carried out using steady state algorithm and the program is considered to reach the final solution when the maximum normalized residual approaches a value of 10^{-4} .

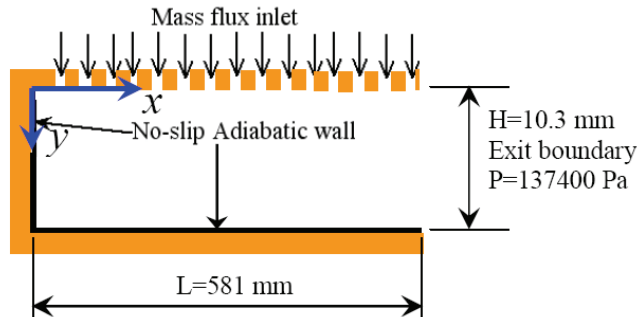
2.2 Near-wall treatment

In the region near the wall, the gradient of quantities is considerably high and requires fine grids close to the wall to capture the change of quantities. This causes the calculation to become more expensive meaning time-consuming, requiring greater memory and faster processing on the computer, as well as expensive in terms of complexity of equations. A wall function, which is a collection of semi-empirical formulas and functions, provides a cheaper calculation by substituting the fine grids with a set of equations linking the solution's variables at the near-wall cells and the corresponding quantities on the wall. For the present simulation, the standard wall function proposed by Launder; Spalding (1974) becomes reliable and simple. The $k - \varepsilon$ models (standard as well as extended model of Chen; Kim (1987)) and the Reynolds stress model employ the wall function model. For the SST $k - \omega$ models, when the low-Reynolds number effects are activated, the near-wall grids have to be very fine to obtain the better results for the near wall modeling.

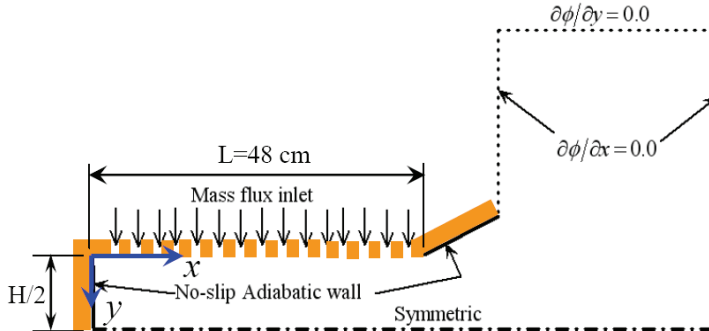
For $v^2 - f$ turbulence model, the wall boundary conditions for ε and f are developed from the near-wall asymptotic behavior of the k and v^2 equations forcing $k \sim (y_p)^2$ and $v^2 \sim (y_p)^4$, respectively, where y_p is measured from the wall. The boundary conditions at the wall have been specified as:

$$k_w = 0; \quad v_w^2 = 0; \quad \varepsilon_p = \frac{2\mu k_p}{\rho(y_p)^2}; \quad f_w = 0.
 \tag{17}$$

The indices w and p denote, respectively, the wall and the first point next to the wall.



(a) The physical model for channel with porous wall at lower side from which an asymmetrical injection is imposed



(b) The physical model for channel ended with a divergent part (Nozzleless Rocket Motor Chamber) with symmetrical injection. (Upper half of the computational domain is only considered, because of the flow symmetry)

Figure 1: Computational domain.

2.3 Boundary conditions

2.3.1 Channel with asymmetric injection

Different boundary conditions are imposed on the computational domain shown in Fig. 1 (a). The value of the mass flux through the porous wall (mass flux = $2.619 \text{ Kg/m}^2 \text{ s}$) as measured by Avalon; Casalis; Griffond (1998) for investigating the characteristics of injection driven flows in a two-dimensional channel of height $H = 10.3 \text{ mm}$ and length $L = 581 \text{ mm}$ is considered. At the porous wall the pressure is extracted from the interior pressure solution using the condition $\partial p / \partial y = 0$ and the experimentally registered temperature of 303 K is used. Appropriate values of k, ε, ω

and v^2 have been prescribed at the porous wall together with streamwise velocity $u = 0$. At the exit section the pressure is 1.374 bar in accordance with operating of the experimental setup. The injection Reynolds number: $Re_s = \rho_s v_s H / \mu_s$, is approximately 1600. No-slip boundary conditions have been assigned on all adiabatic solid walls and extrapolation boundary condition has been employed at the outflow except the pressure which has given a constant prescribed value as previously discussed. It must be noted that a value of f must be specified at the injection boundary. The calculation considered in the present work has been performed imposing $f = 1$ on the porous wall.

Because of sensitivity of results to the grid resolution, a grid dependence study has been conducted. Three grids levels have been used with 150×150 , 200×200 and 250×250 grid points in the axial and vertical direction, respectively. It has been found that no noticeable modifications in the mean velocity as well as the turbulent stresses with introducing the finest grid, so all computations have been carried out using the mid grid of 200×200 grid points, which produces a near-wall dimensionless distance of y^+ value of order 0.8 along the grid line closest to the wall. The grid is then smoothly expanded to the core using a suitable expansion factor.

2.3.2 Channel with symmetric injection (nozzleless rocket motor chamber)

A schematic representation of the nozzleless rocket motor considered in this activity is shown in Fig. 1 (b). This is a 2-D planar, porous walled duct closed at one end and with a divergent section with impermeable walls at the other end. The cylindrical port chamber has a length of $L=48$ cm, a height of $H=2$ cm; the diverging part has a length of 3.2 cm and a semi-angle equal to 15 degrees; the expansion area ratio is 1.86. Air at a temperature of 260 K and a pressure of 8 bar was used in the experiments of Traineau; Hervat; Kuentzmann (1986). Large injection flow rates were attained in these tests: the injection mass flux was equal to $13(\text{kg}/\text{sec})/\text{m}^2$, while the injection Reynolds number was 7840; these represent typical values for solid rocket motors; the mean flow Reynolds number based on throat conditions was approximately, 1.5×10^6 . Experimental data available at five axial stations along the cylindrical duct including: static pressure measurements, mean velocity profiles, turbulence intensity, and Reynolds stress profiles. The considered stations read $x/h = 12; 24; 30; 40$ and 46 , respectively, where $h = H/2 = 1\text{cm}$.

3 Results and discussions

3.1 Channel with asymmetric injection

The mean velocity and the Reynolds-stress profiles are compared with that measured at eight sections of the channel located at $x = 31; 120; 220; 350; 400; 450; 500$ and 570mm . This is corresponding to dimensionless distances $x/H = 3; 11.65; 21.36; 33.98; 38.83; 43.69; 48.54$ and 55.34 , respectively. Figure 2 shows the mean streamwise velocity profiles normalized by the local mean streamwise velocity U_m , where $U_m = \frac{1}{H} \int_0^H u dy$. The numerical results of the different turbulence models used are compared with the experimental data of Avalon; Casalis; Grifond (1998) in global coordinates y/H . As noticed, the velocity increases rapidly in the boundary layer generated on the solid wall compared with that on the porous wall. The failing of all turbulence models to predict the velocity at the first location $x = 31\text{mm}$ may be due to the presence of a laminar flow in this zone. Chaouat (2002) found numerically that the transition from laminar to turbulent flow is located at $x \approx 410\text{mm}$ on the permeable wall and $x \approx 200\text{mm}$ on the impermeable wall. The turbulence models used predict qualitatively the velocity profiles at all other locations.

However, it is noticed that SST $k - \omega$, RSM and $v^2 - f$ turbulence models reproduce the best agreement with the experimental data compared with the other used turbulence models. The standard $k - \epsilon$ turbulence model and its extended form of Chen; Kim (1987) represent only the core flow and clear deviations are observed near the two wall in spite of the absence of adverse pressure gradient in the present simulation case, i.e., the failure of the turbulence models used near wall is not caused by the near-wall treatment, but can be produced by the isotropic assumptions in the turbulence model itself. The certain response of the SST $k - \omega$ turbulence model, which is a mixture of the standard $k - \epsilon$ and $k - \omega$, to remedy this failure is a noticeable result. However, larger deviations have been previously obtained using RSM model by Chaouat (2002).

The computed axial pressure distributions along the solid wall with different turbulence models are reported in Fig. 3, where P is the static pressure, while P_o is the stagnation pressure. Similar results are obtained from RSM, SST $k - \omega$ and V2F turbulence models, while stronger pressure gradient near the channel exit is predicted by the standard and the extended Chen-Kim $k - \epsilon$ turbulence models.

A more definitive way to determine the axial location of the mean flow transition from laminar to turbulent flow consists in examining the local variation of the wall skin-friction coefficient defined as: $C_f = 2(u_\tau/U_m)^2$, where u_τ is the local computed wall shear velocity. Figure 4 shows the development of the local wall skin-friction coefficient computed for the solid wall. As can be seen, the rapid in-

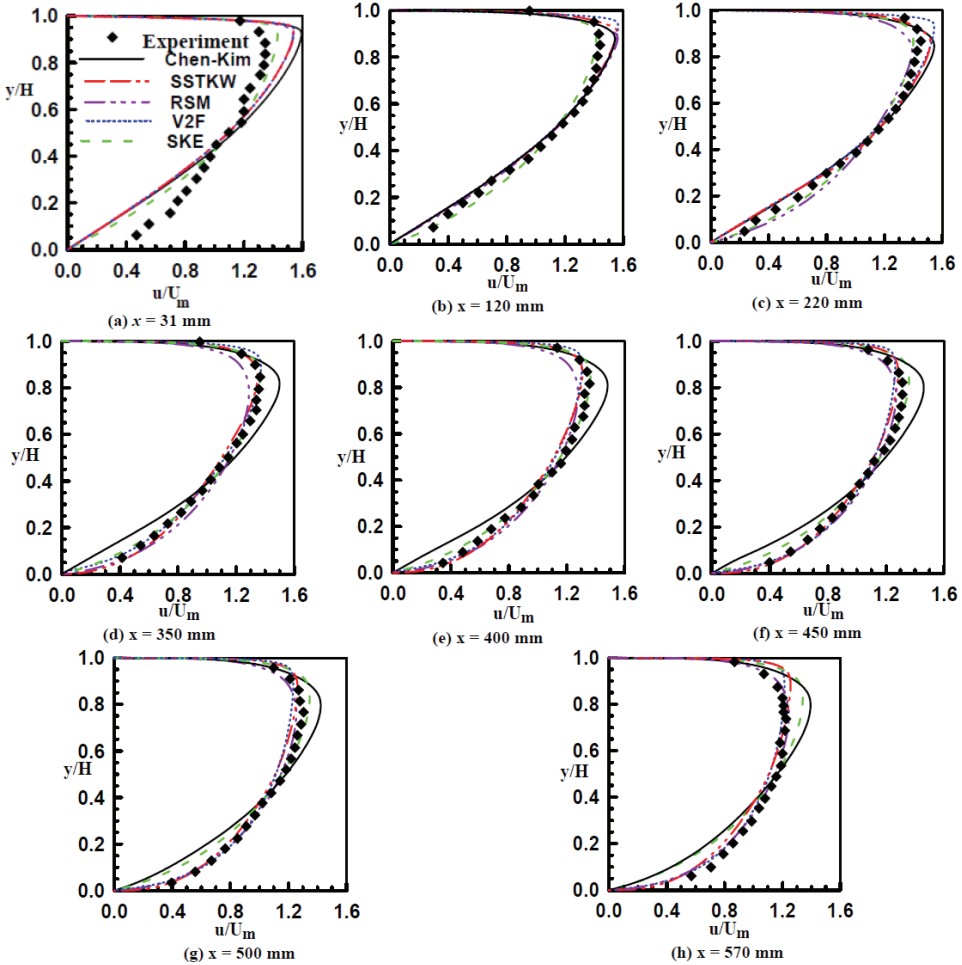


Figure 2: Mean velocity profiles at different locations (Symbols: Experimental data (symbols) of Avalon; Casalis; Griffond (1998)).

crease in the profile of the skin friction coefficient reveals the location of transition, which can be only observed from the numerical prediction of the V2F turbulence model, while there is no explicit clear transition predicted by the other used turbulence models. The laminar code solution developed by the present authors is also included in the figure to show the behavior of the turbulence models in the regions of low Reynolds numbers. However, the most successful model approaching to the results of the V2F is the SST $k - \omega$ turbulence model. Over-prediction is clearly observed from the results of the other turbulence models used due to the higher

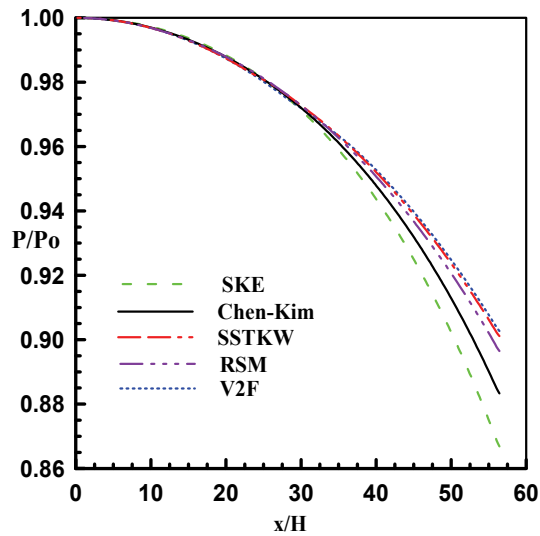


Figure 3: Predicted axial pressure distribution on the solid wall using different turbulence model.

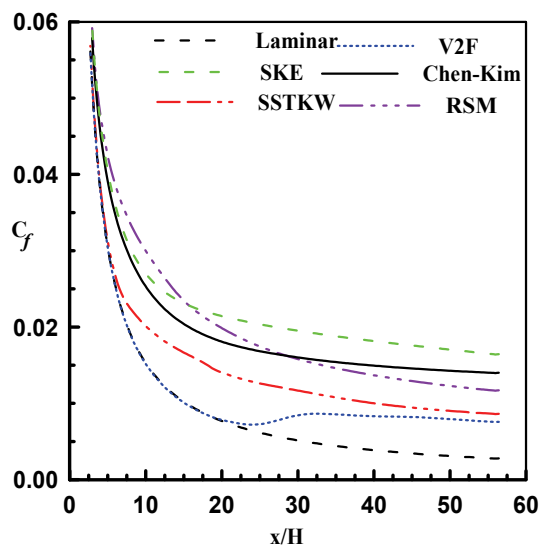


Figure 4: Predicted axial variation of the skin-friction coefficient on the solid wall using different turbulence models.

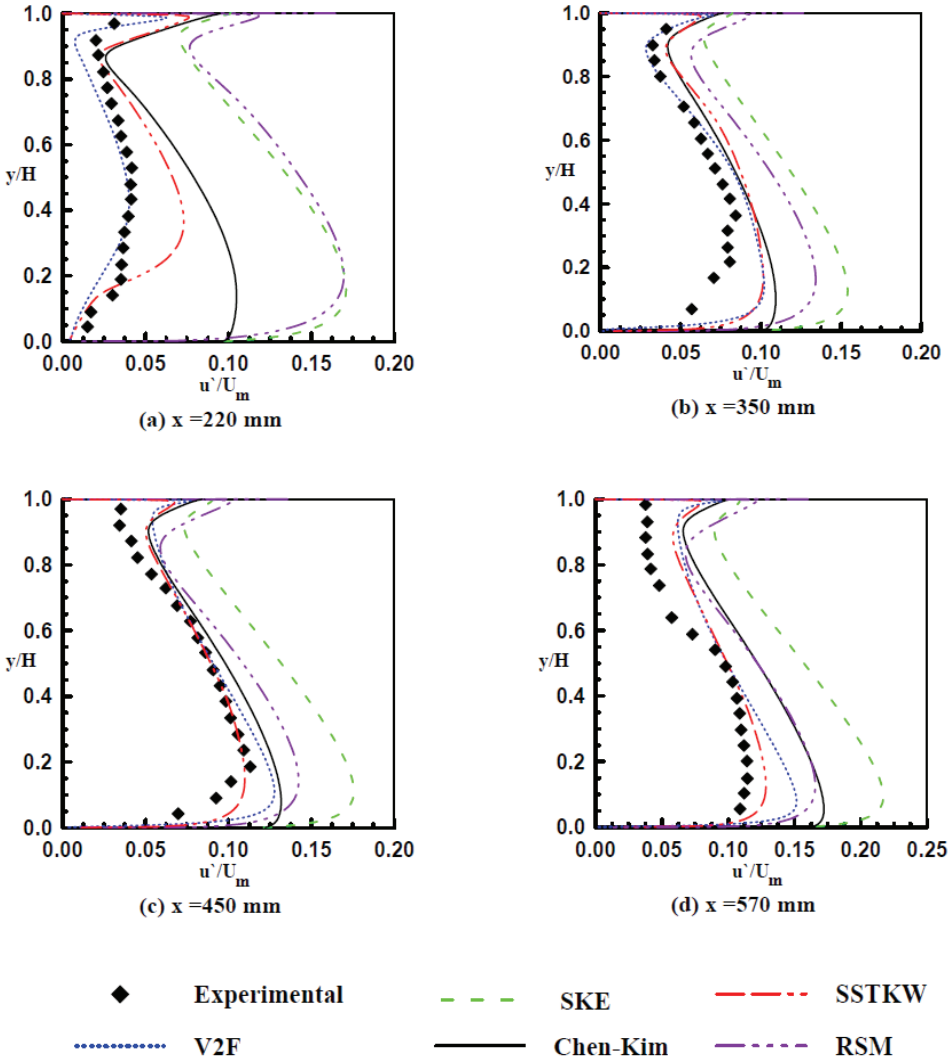


Figure 5: Streamwise root-mean-square (RMS) turbulence intensity at different locations.

pressure gradient predicted with using those turbulence models.

Figure 5 describes the streamwise root-mean-square (RMS) turbulence intensity u' normalized by the local bulk streamwise velocity U_m at four locations reading: $x = 220$; 350 ; 450 and 570 mm, respectively. It is apparent that there are always peaks in the profiles near the porous wall surface. That is clearly visible in the

experimental and numerical data. The known near-wall stress peaks at the other solid wall due to the boundary layer development and the strong near-wall velocity gradient couldn't be experimentally captured, while they are numerically observed in all turbulence models used. Except the first location, that is at near of the transition from laminar to turbulent flow, all turbulence models present qualitatively good agreement with the experimental data.

The higher levels observed in the near-wall turbulence intensity are probably due to the pseudo-turbulence of the injected flow. However, all computations predict somewhat higher values of turbulence intensity compared with the experimental data. The SST $k - \omega$ and $v^2 - f$ turbulence models still reproduce the best predictions compared with the other turbulence models used.

Figure 6 shows the normal root-mean-square (RMS) turbulence intensity v' normalized by the local bulk streamwise velocity U_m at the same previously mentioned four locations. It is clear that the normal component is well reproduced by the Reynolds-stress model, although minor discrepancies with the experimental data are observed for the first location where there is a predicted transition from laminar to turbulent flow. However, the predicted normal stress component with near-wall peaks near the solid wall doesn't agree well with the experimental data also as discussed previously in the streamwise component. This disagreement could be attributed to the measurements itself that are not accurate in the vicinity of the solid wall because the hot-wire probe used to measure the turbulence intensity components is introduced through this wall, see Avalon; Casalis; Griffond (1998) and Chaouat (2002). Generally, the intensity of the turbulence velocity fluctuations in the streamwise direction is higher than that in the direction normal to the wall.

Chaouat (2002) repeated the computation of the turbulent velocity fluctuations at different cross sections of the channel using the standard $k - \epsilon$ turbulence model incorporating damping functions. The numerical results obtained by Chaouat (2002) overpredict strongly the experimental results of Avalon; Casalis; Griffond (1998). These overpredictions may be due to the very fine near-wall grid used by Chaouat (2002).

The turbulent shear stress component $u'v'/U_m^2$ is presented at the given locations is seen in Fig. 7. Good results are obtained from SST $k - \omega$ and $v^2 - f$ turbulence models.

Figure 8 presents contours plot of turbulent kinetic energy. A large amount of turbulence is concentrated near the porous wall/channel exit above it; this clearly shows that the level of turbulence is higher when entrainment of the injected fluid is happening.

The contours of the computed Mach number in the computational domain are

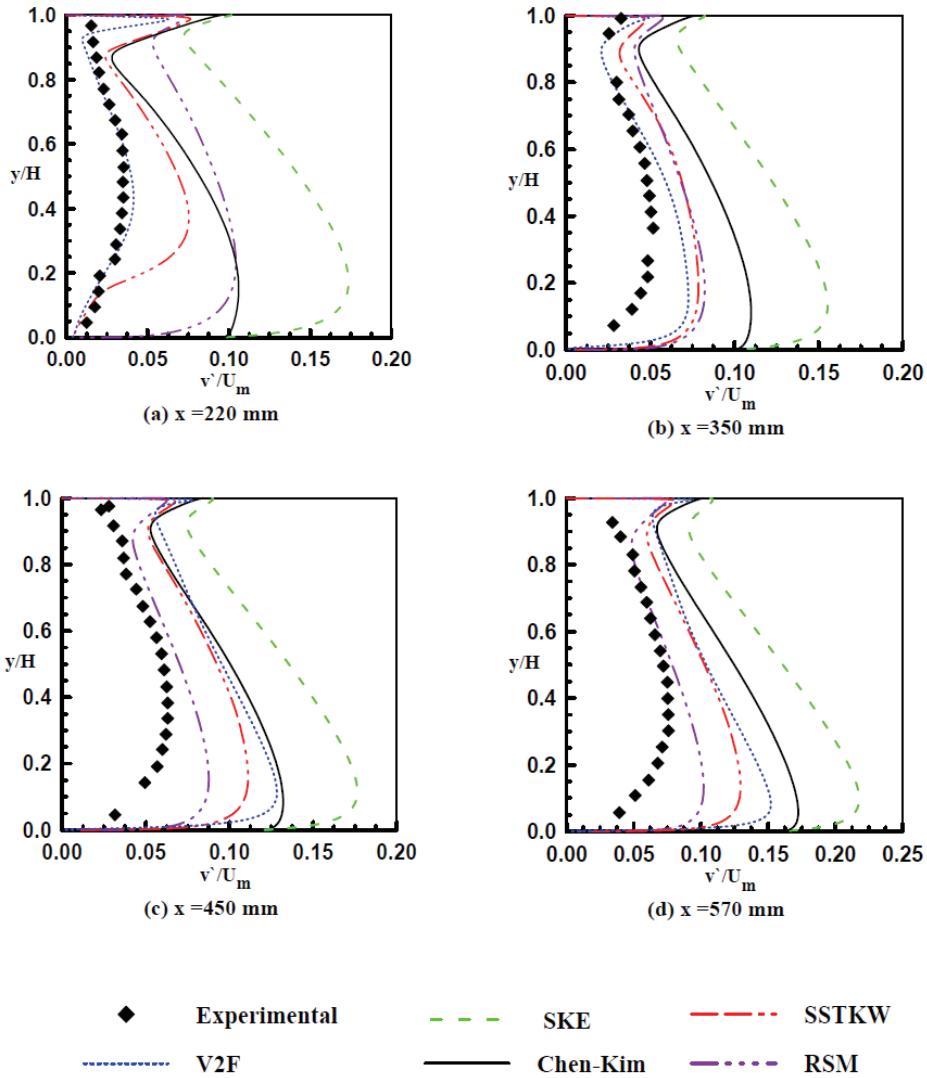


Figure 6: Vertical root-mean-square (RMS) turbulence intensity at different locations.

shown in Figure 9. It is clearly visible that the maximum Mach number reached in the present study is 0.32, with the highest values approaching to the solid wall/exit of the channel. This was clearly noticed in the velocity profiles discussed previously with higher momentum near the solid wall, because of the strong displacement thickness development near the porous wall which leads to a high convective

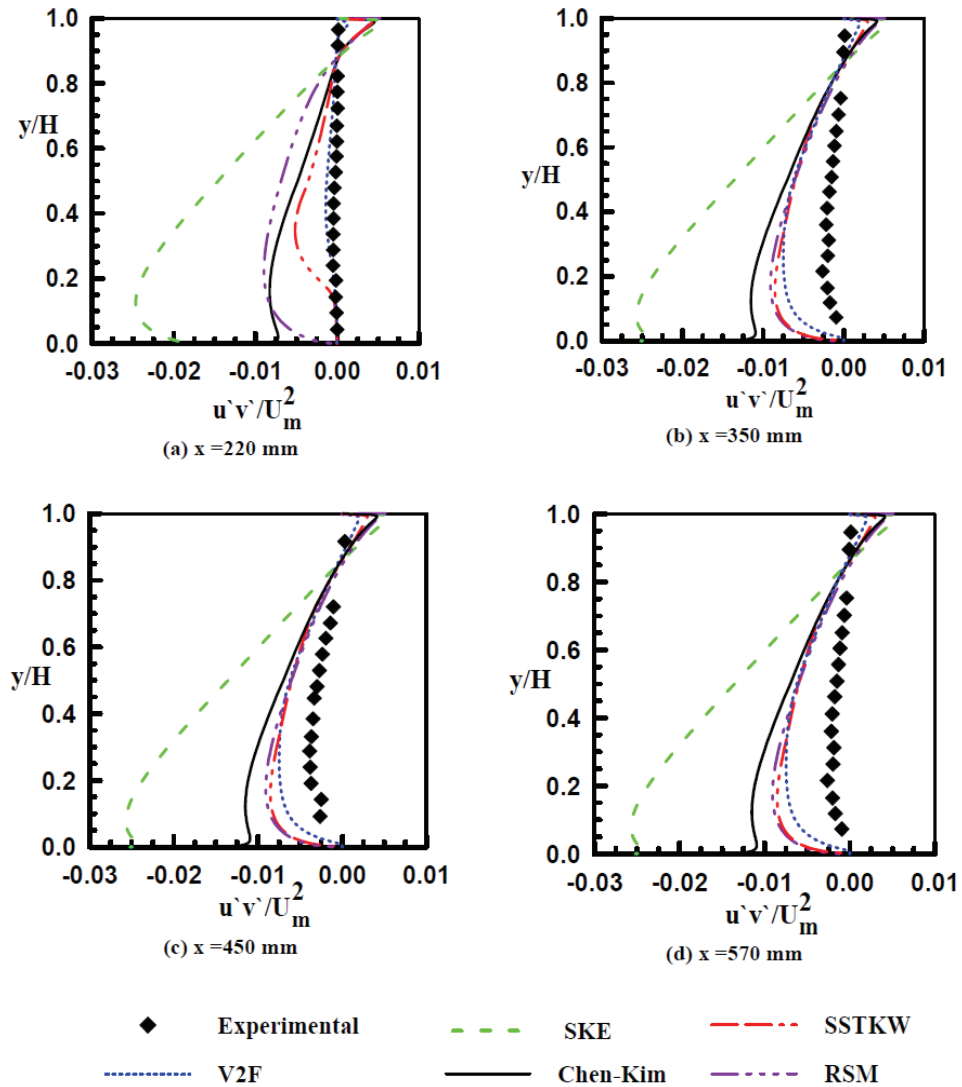


Figure 7: Turbulent shear stress at different locations.

mass transfer to the solid wall. The Mach number contours shows that injection of fluid through the porous wall has the effect of reducing the flow Mach number near the porous wall.

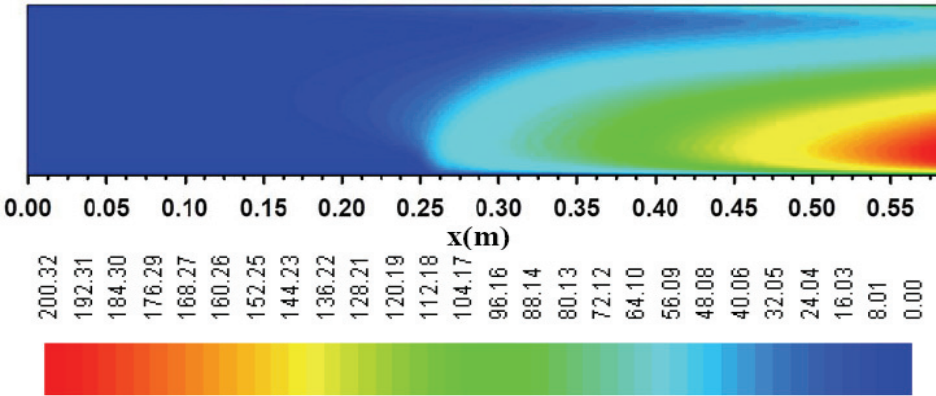


Figure 8: Turbulence kinetic energy contours plot (m^2/s^2).

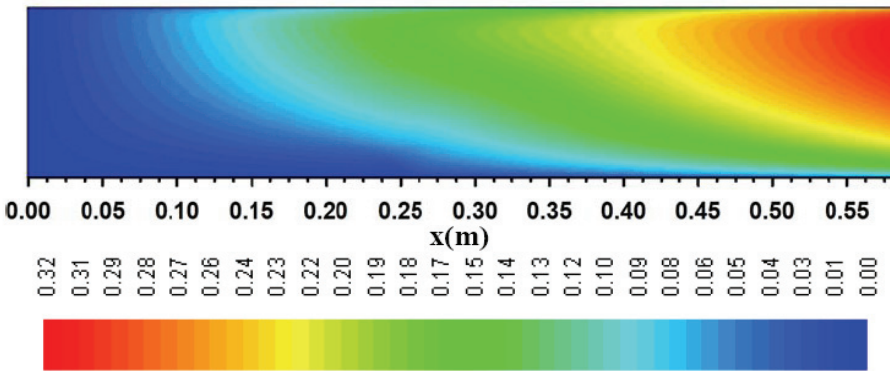


Figure 9: Computed Mach number contours plot

3.2 Nozzleless rocket motor chamber

Computations of the flow in this nozzleless duct were previously performed using full compressible Navier-Stokes equations together with the $v^2 - f$ and low-Reynolds $k - \epsilon$ turbulence models, see Ciucci; Iaccarino; Moser; Najjar; Durbin (1998) in a computer code CFL3D. In our simulation, the code is developed by the present authors with implemented different turbulence models. For the present simulation case, only the $v^2 - f$ turbulence model is used, because of its simplicity and the good results obtained.

The computed pressure distributions along the motor centerline are compared with the experimental values in Fig. 10. As noticed, a strong pressure gradient is present

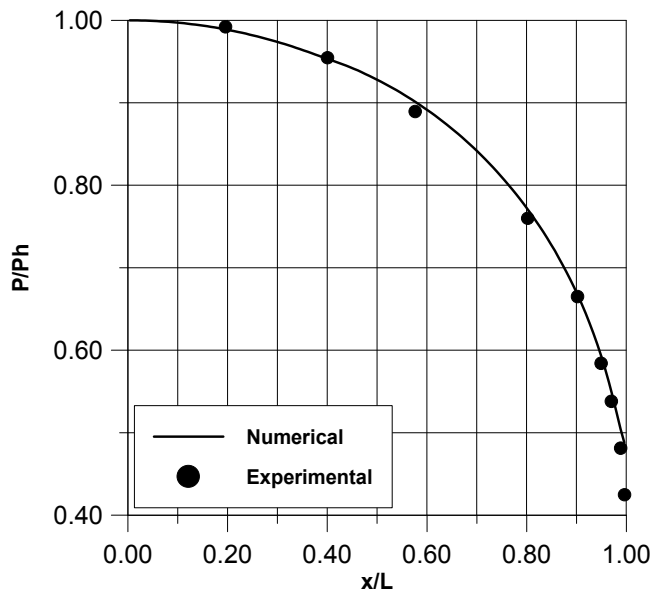


Figure 10: Comparison between predicted axial pressure distribution with experimental data (symbols) of Traineau; Hervat; Kuentzmann (1986).

in the channel, and compressibility effects become relevant in the second half of the channel.

The axial u -velocity distributions along the centerline ($y/h = 1$) and near the wall at $y/h = 0.1$ are experimentally and numerically represented in Fig. 11. The results show good predictable turbulence model.

A comparison of the velocity profiles with the experimental data of Traineau; Hervat; Kuentzmann (1986) is reported in Fig. 12. In the two initial stations, predicted profiles lie below the experimental values: at $x/h = 19$ the computed velocity profile approximates very well Culick's inviscid distribution while at $x/h = 28.5$ the profiles start to transition toward a "fuller" profile; a full transition has occurred nearly at $x/h = 30$ and a turbulent velocity profile is attained more downstream. The $v^2 - f$ turbulence model predicts slightly lower values than those measured by Traineau; Hervat; Kuentzmann (1986). Generally, good predictions are obtained from the used turbulence model, representing the velocity and the pressure.

However, this is not sufficient to verify a turbulence model. The turbulence energy representation approaches to the decision of turbulence model quality. Figure 13 shows the profiles of the turbulence intensity (\sqrt{k}) at the mentioned axial locations. As observed the numerical results give the similar trends of the experimental data.

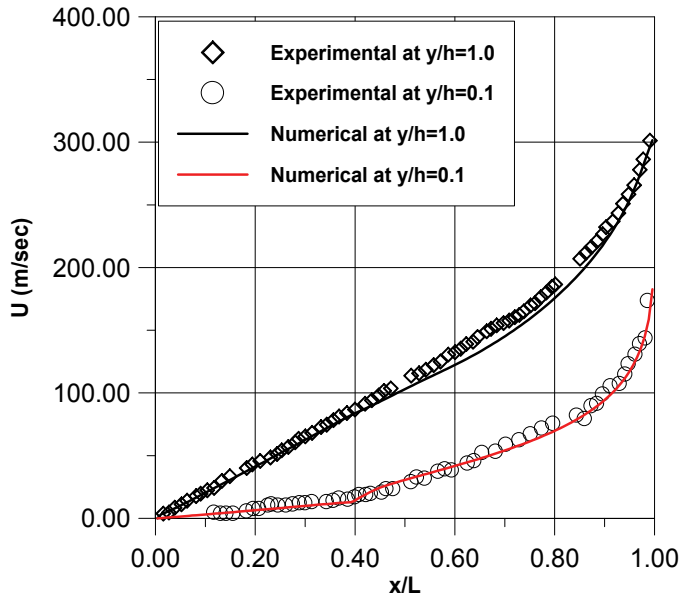


Figure 11: Comparison between predicted axial velocity distribution with experimental data of Traineau; Hervat; Kuentzmann (1986) at two vertical levels.

However, larger discrepancies with the experimental data are observed in the turbulent kinetic energy profiles computed in Ciucci; Iaccarino; Moser; Najjar; Durbin (1998), while the present numerical results show good comparisons. The higher experimental levels observed in the initial part of the channel are probably due to the "pseudo turbulence" of the injected flow; as reported by Traineau; Hervat; Kuentzmann (1986) transition to turbulence occurs between $x/h=20$ and $x/h=30$, and the flow becomes fully turbulent beyond this location. The computations predict a somewhat faster transition with higher k values within most of the channel: an overprediction slightly less than 100% is observed in the middle of the channel; this overprediction tends to decrease at locations more downstream.

The turbulence model used predicts somewhat higher peak values and closer to the wall than the experimental data. The differences between computed and measured values may be due both to the turbulence of the injected fluid and to transition effects.

4 Conclusions

Computations are performed to investigate the nature of a compressible flow in a 2D channel with symmetric and asymmetric injection through a porous wall. The

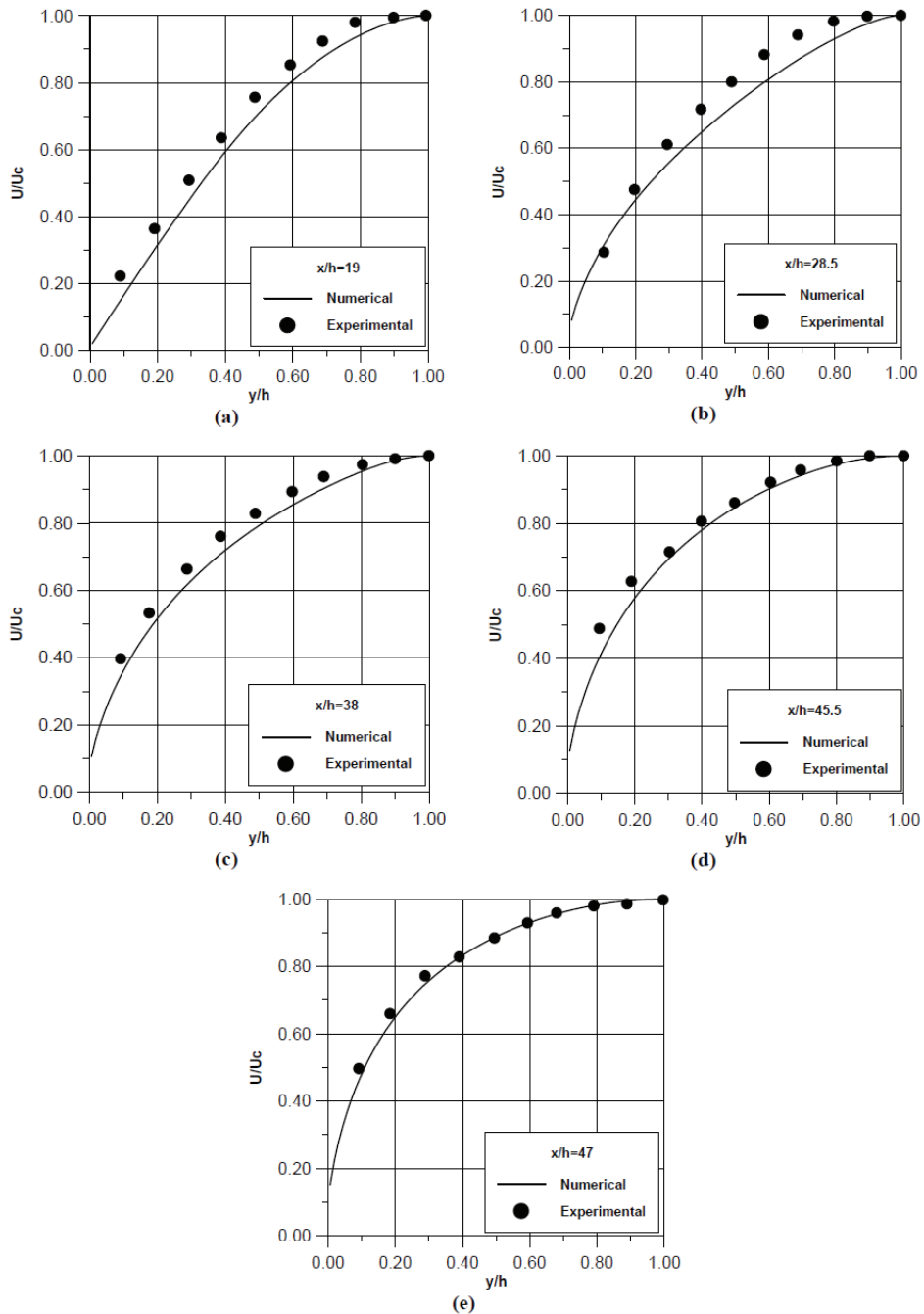


Figure 12: Comparison between predicted axial velocity distributions with experimental data of Traineau; Hervat; Kuentzmann (1986) at different axial locations.

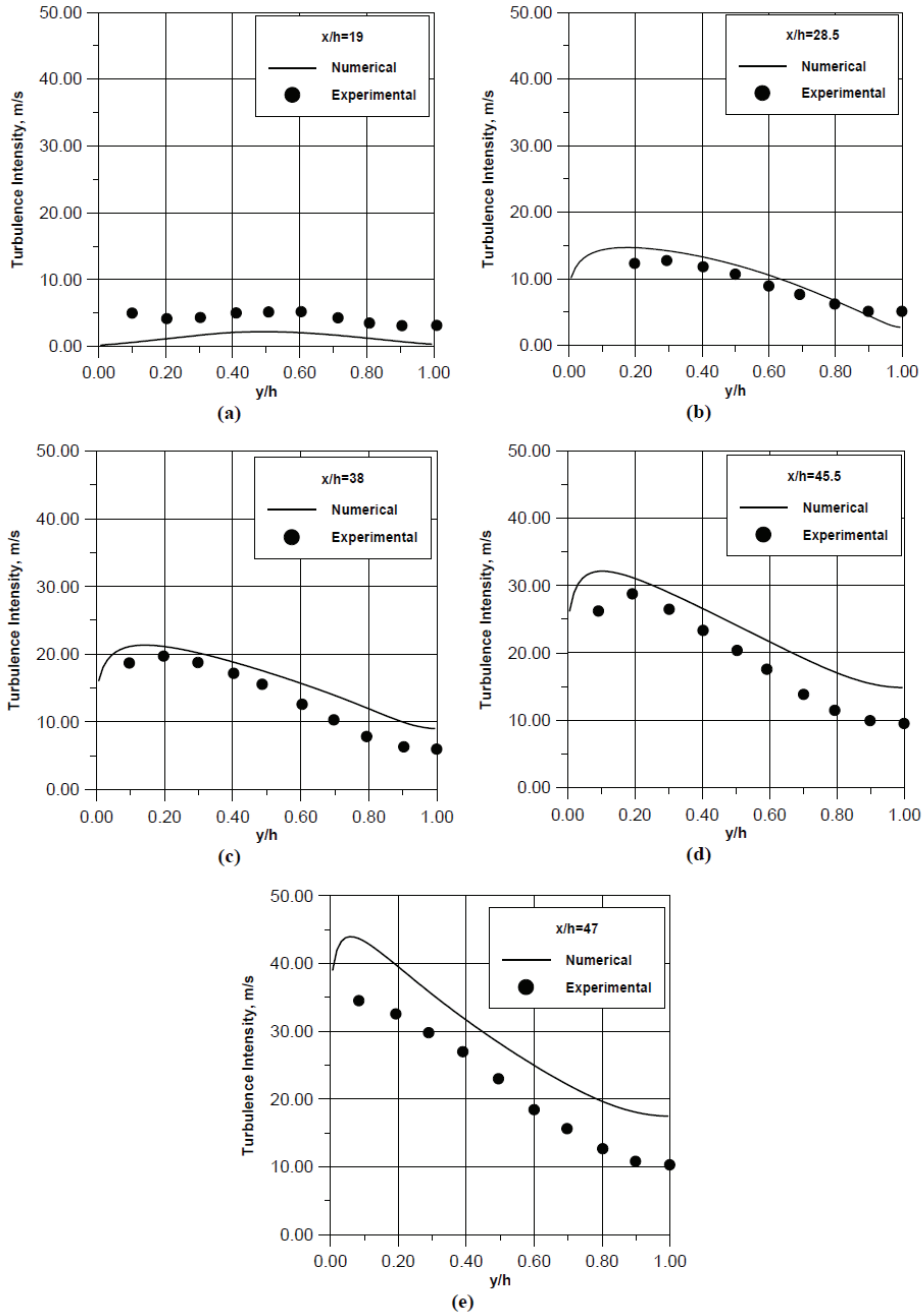


Figure 13: Comparison between predicted turbulence intensity (\sqrt{k}) distributions with experimental data of Traineau; Hervat; Kuentzmann (1986) at different axial locations.

simulations are performed using different turbulence models. A comprehensive comparison between these models and the available experimental results is performed. In general, the numerical calculation results represented by the calculated mean axial velocity show fairly good agreement with experimental data. Two of these models, SST $k - \omega$ and $v^2 - f$ turbulence models show the smallest deviation with the experimental results followed by the RSM model, while the SKE model shows the largest deviation with the experimental one. Because of the presence of impermeable and permeable walls, the development of turbulence has occurred at two different locations in the channel. Both SST $k - \omega$ and $v^2 - f$ turbulence models largely over-predicted the measured values of the Reynolds stresses. The correct capture of transition from laminar to turbulent flow in the duct explains most success of the $v^2 - f$ turbulence model in simulation of such configuration with side-wall injection and the discrepancy observed as well as the difference in the predictions of the other turbulence models. The present flow prediction reveal that the turbulence is developed more rapidly near the impermeable wall compared with the little bit variation near the porous wall.

The activities conducted in this work indicated that the results achieved are very encouraging, which should foster a more extensive research in this field. More extensive investigation of the applicability of the $v^2 - f$ turbulence model to this kind of flow is needed before any definite conclusion may be drawn. However, a future work is planned to apply the nonlinear turbulence models previously tested in much more complex flow by El-Askary; Balabel (2007) and Balabel; El-Askary (2011). Also, the divergent part at the end of the duct will be replaced by a convergent-divergent nozzle with the presence of different injection mass flux to control the presence or absence of generated shock wave.

Acknowledgement: This work is financially supported by the Science and Technology Development Fund (STDF) through the contract ID-108.

References

Andersen, P.S.; Kays, W.M.; Moffat, R.J. (1975): Experimental results for the transpired turbulent boundary layer in an adverse pressure gradient. *J. Fluid Mechanics*, vol. 69, pp. 353-375.

Apte, S.; Yang, V. (2001): Unsteady flow evolution in porous chamber with surface mass injection, Part 1: Free oscillation. *AIAA J.*, vol. 11 (8), pp. 1577-1586.

Avalon, G.; Casalis, G.; Griffond, J. (1998): Flow instability and acoustic resonance of channels with wall injection. *AIAA Paper* 98-3218.

Balabel, A; El-Askary, W.A. (2011): On the performance of linear and nonlin-

ear $k-\varepsilon$ turbulence models in various jet flow applications. *European Journal of Mechanics B/Fluids*, vol. 30, pp. 325-340.

Beddini, R.A. (1986): Injection-induced flows in porous-walled ducts. *AIAA J.*, vol. 24 (11), pp. 1766-1773.

Chaouat, B. (2002): Numerical predictions of channel flows with fluid injection using Reynolds-Stress Model. *J. Propulsion and Power*, vol. 18 (2), pp. 295-303.

Chen, Y.S.; Kim, S.W. (1987): Computation of turbulent flows using an extended $k - \varepsilon$ turbulence closure model. *Int. Report NACA-CR-179204*.

Ciucci, A.; Iaccarino, G.; Moser, R.; Najjar, F.; Durbin, P. (1998): Simulation of rocket motor internal flows with turbulent mass injection. *Center for Turbulence Research, Proceedings of the Summer Program*, pp. 245-266.

Culick, F.E.C. (1966): Rotational axisymmetric mean flow and damping of acoustic waves in solid propellant rocket motors. *AIAA J.*, vol. 4 (8), pp. 1462-1464.

Dunlap, R.; Blackner, A.M.; Waugh, R.C.; Brown, R.S.; Willoughby, P.G. (1990): Internal flow field studies in a simulated cylindrical port rocket chamber. *J. Propulsion and Power*, vol. 6 (6), pp. 690-704.

Dunlap, R.; Willoughby, P.G.; Hermsen, R.W. (1974): Flow field in the combustion chamber of a solid propellant rocket motor. *AIAA J.*, vol. 12 (10), pp. 1440-1442.

Durbin, P.A. (1995): Separated flow computations with $k - \varepsilon - v^2$ model. *AIAA J.* vol. 3 (4), pp. 659-664.

El-Askary, W.A.; Balabel, A. (2007): Prediction of reattaching turbulent shear flow in asymmetric divergent channel using linear and non-linear turbulence models. *Engineering Research Journal (ERJ)*, Faculty of Eng., Menoufiya University, vol. 30 (4), pp. 535-550.

Hinze, J.O. (1975): *Turbulence*. McGraw-Hill Publishing Co., New York.

Jones, W.P.; Launder, B.E. (1972): The prediction of laminarization with a two-equation model of turbulence. *Int. J. of Heat and Mass Transfer*, vol. 15, pp. 301-314.

Launder, B.E.; Reece, G.J.; Rodi, W. (1975): Progress in the development of a Reynolds-stress turbulence closure. *J. Fluid Mechanics*, vol. 68 (3), pp. 537-566.

Launder, B.E.; Spalding, D.B. (1974): The numerical computation of turbulent flows. *J. Computer Methods in Applied Mechanics and Engineering*, vol. 3, pp. 269-289.

Lien, F.S.; Kalitzen, G. (2001): Computation of transonic flow with the $v^2 - f$ turbulence model. *International Journal of Heat and Fluid Flow*, vol. 22, pp.

53-61.

Liou, T.M.; Lien, W.Y. (1995): Numerical simulations of injection-driven flows in a two-dimensional nozzleless solid rocket motor. *J. Propulsion and Power*, vol. 11 (4), pp. 600-606.

Liou, T.M.; Lien, W.Y.; Hwang, P.W. (1998): Transition characteristics of flow field in a simulated solid rocket motor. *J. Propulsion and Power*, vol. 14 (3), pp. 282-289.

Menter, F.R. (1994): Two-equation eddy-viscosity turbulence models for engineering applications. *AIAA J.* vol. 32 (8), pp. 1598-1605.

Moin, P. (1982): Numerical simulation of wall-bounded turbulent shear flows. *Proceedings of the 8th International Conference on Numerical Methods in Fluid Dynamics*, Edited by E. Krause, Springer-Verlag, New York, pp. 55-76.

Patankar, S.V. (1980): *Numerical heat transfer and fluid flow*. Hemisphere Publishing Corporation.

Pecnik, R.; Iaccarino, G. (2007): Predictions of turbulent secondary flows using the $v^2 - f$ model. *Center for Turbulence Research, Annual Research Briefs*, pp. 333-343.

Piomelli, U.; Moin, P.; Ferziger, J. (1991): Large eddy simulation of the flow in a transpired channel. *J. Thermophysics*, vol. 5 (1), pp. 124-128.

Sabnis, J.S.; Gibeling, H.J.; McDonalds, H. (1989): Navier-Stokes analysis of solid propellant rocket motor internal flows. *J. Propulsion and Power*, vol. 5 (6), pp. 567-664.

Sabnis, J.S.; Madabhushi, R.; Gibeling, H.J.; McDonalds, H. (1989): On the use of $k-\epsilon$ turbulence model for computation of solid rocket internal flows. *AIAA 89-558, 25th Joint Propulsion Conference*, Monterey, CA.

Traineau, J.C.; Hervat, P.; Kuentzmann, P. (1986): Cold-flow simulation of a two-dimensional nozzleless solid rocket motor. *AIAA 86-1447, 22nd Joint Propulsion Conference*, Huntsville, AL.

Wilcox, D.C. (1998): *Turbulence modeling for CFD*. DCW Industries, Inc., La Canada, California.